Analytical Methods

ROYAL SOCIETY OF CHEMISTRY

PAPER

View Article Online
View Journal | View Issue

Cite this: *Anal. Methods*, 2025, **17**, 8413

Conversion of biomass into porous carbon materials for efficient electrochemical detection of ornidazole

Chang Liu,[a] Tianlong Shan,[b] Yuxiang Yang,[c] Mengmeng Ding*[d] and Rui Zhang *[e]

The conversion of biomass into high-value carbon materials presents significant opportunities for electrochemical sensing due to their large specific surface area, abundant pore structure as well as prominent electrical conductivity. In this study, a high-performance electrochemical sensor based on waste biomass was developed for the rapid detection of ornidazole (ODZ). After systematically screening various biomass materials, including crab shell, pine nut shell, pig bone, and mandarin orange peel along with their respective activation methods, it was determined that H_3PO_4-activated pine nut shell (**P-PNS**) served as the optimal precursor. Under a nitrogen atmosphere, the porous biomass derived carbon material **P-PNS-800** was synthesized by heating at a rate of 5 °C min^{-1} to 800 °C and maintaining it for 2 hours. The morphological and structural characteristics of pine nut shell-derived carbon at varying pyrolysis temperatures were analyzed using SEM, XRD, FT-IR and nitrogen adsorption–desorption techniques. The results demonstrated that during high-temperature carbonization, the synergistic effects of lignin decomposition and polyphosphate bond volatilization led to the formation of a highly defective carbon skeleton with a specific surface area of 1317.84 m^2 g^{-1}. The material exhibited superior electrocatalytic performance toward ODZ, obtaining a wide linear range of 0.20–150 μM, a high sensitivity of 0.48 μA $μM^{-1}$, and a limit of detection as low as 0.05 μM (S/N = 3). When applied to ornidazole tablets, the results were in good accordance with those obtained by HPLC, confirming the promising application potential of biomass-derived carbon materials in the field of electrochemical sensing. This work offers a significative strategy for the utilization of waste resources and the detection of antibiotics.

Received 30th June 2025
Accepted 21st September 2025

DOI: 10.1039/d5ay01069a

rsc.li/methods

1. Introduction

Ornidazole [ODZ, 1-(3-chloro-2-hydroxy) propyl-2-methyl-5-nitroimidazole)] is a third generation nitroimidazole derivative newly synthesized following metronidazole and tinidazole, which has more significant efficacy, shorter duration, and stronger tolerance and has been increasingly used in clinical treatment.[1,2] The structure of ODZ contains a chiral carbon atom with a hydroxyl group, so it has optical activity, and the racemes are S-ODZ and R-ODZ.[3] The elimination of S-ODZ is faster than that of R-ODZ, which significantly reduces the incidence of total clinical adverse reactions of S-ODZ, while R-ODZ is prone to neurotoxicity.[4] Ornidazole is widely used to treat infectious diseases caused by *Clostridium difficile*, *Escherichia coli*, *Streptococcus aureus* and *Helicobacter pylori* by interfering with DNA synthesis of bacteria to achieve bactericidal effects.[5,6] However, overuse can also cause side effects such as abdominal discomfort, vomiting, nausea, and diarrhea.[7,8] Therefore, it is necessary to build an accurate and efficient ODZ content detection method in the clinical and pharmaceutical assay. Over the past few decades, determination of ODZ was carried out by various traditional methods such as luminescence,[9] high performance liquid chromatography (HPLC),[10] fluorescence[11] and capillary electrophoresis.[12] However, these methods have been proven to be time-consuming, involving costly equipment and complex sample preparation protocols, and technicians are required to complete the operation.[13,14] Compared with other techniques, electrochemical sensing technology shows unique advantages in the field of drug analysis, with high sensitivity, strong specificity, a low detection limit and easy operation.[15,16] In particular, the reaction mechanism and pharmacological activity of ODZ can be understood by electrochemical analysis methods.[17]

[a]*College of Criminal Science and Technology (College of Forensic Science), Criminal Investigation Police University of China, Shenyang 100854, P. R. China*
[b]*Organization of Personnel Division, Criminal Investigation Police University of China, Shenyang 100854, P. R. China*
[c]*College of Police Dog Technology, Criminal Investigation Police University of China, Shenyang 110000, P. R. China*
[d]*Department of Anaesthesiology, Shengjing Hospital of China Medical University, Shenyang 110004, P. R. China. E-mail: ivy_ding@126.com; Tel: +86-24-62215711*
[e]*Shenyang Key Laboratory of Medical Molecular Theranostic Probes in School of Pharmacy, School of Pharmacy, Shenyang Medical College, Shenyang, 110034, P. R. China. E-mail: ruizhang@lnu.edu.cn*

Generally, electrode materials play a crucial role in determining the performance of electrochemical detection. The development of highly efficient electrode materials for the detection of ODZ is therefore highly desirable. Zhou *et al.* developed cobalt-supported nitrogen-doped carbon nanocages (Co@CN-CNTs) derived from metal–organic frameworks, which enable sensitive electrochemical detection of ODZ across a broad range from 60 nM to 45 μM.[18] Similarly, Cao *et al.* designed a bimetallic CuFe layered double hydroxide supported on carbon black as an electrocatalyst for ODZ detection, achieving an extensive detection range of 0.01–260 μM and a low detection limit of 7.6 μM.[5] Although these carbon-based electrode materials for ODZ electrochemical sensing demonstrate commendable detection capabilities, their preparation processes are relatively complex and necessitate the involvement of metal ions. In comparison, biomass is regarded as a renewable energy source, ranking second only to traditional energy sources like coal, gasoline, and natural gas in terms of resource abundance.[19] Biomass can be converted into many types of carbon materials through different technical processes, and their characteristics such as porosity, surface area and conductivity have significant impacts on electrochemical sensor performance.[20,21]

The one-step high temperature pyrolysis of reproducible biomass establishes a new approach for the synthesis of porous carbon nanomaterials.[22,23] On the one hand, it converts biomass waste into value-added products, which would reimburse the expense of waste management or disposal. On the other hand, when utilizing biomass sources, the biomass materials may comprise various elements in variable proportions, which can potentially be employed as dopants or for the synthesis of composite materials. In addition, as the intrinsic structure of the biomass precursors significantly influences the microstructure and porosity of carbonized products, a diverse range of carbon nanomaterials with biomimetic microstructures and morphologies can be obtained through the deliberate selection of biomass precursors.[24] Thus, biomass carbon offers notable advantages in terms of cost-effectiveness and environmental safety when compared to electrode materials such as metal oxides and metal–organic frameworks.[25] Carbon materials are the mainstream active components for the electrodes of electrochemical sensing.

In this study, we systematically selected four representative biomass wastes: crab shell (CS, serving as a source of chitin/N-dopant), pine nut shell (PNS, as a source of cellulose or lignin), pork bone (PB, providing hydroxyapatite), and mandarin orange peel (MP, acting as a source of pectin and natural heteroatoms). This selection was based on their abundance, sustainability, and particularly their diverse chemical compositions. The biomass source with the optimal detection performance for ODZ was found to be PNS, and the method of activating pine nut shell biomass carbon was further optimized. The effect of carbonation temperature on the composition and morphology of pine nut shell was systematically discussed. Finally, a new electrochemical sensor was prepared, utilizing **C-PNS-800**, which was synthesized through carbonation at 800 °C, as the electrocatalyst for the detection of ODZ. This sensor demonstrates an extensive linear range and a low detection limit for ODZ analysis. This research contributes significant value to expanding the application of green and environmentally friendly materials in the domain of electrochemical sensing.

2. Experimental

2.1. Pyrolysis and activation of biomass

Four biomass sources were selected including CS, PNS, PB, and MP. First, the biomasses were cleaned with deionized water, and dried at 80 °C for 48 hours. Then, the pyrolysis was conducted in a quartz tube furnace at 800 °C with a heating rate of 5 °C min^{-1} and kept for 2 hours under a nitrogen atmosphere. After the samples were cooled down, the samples were crushed into a fine powder, sieved through a 50-mesh, followed by rinsing with deionized water three times and finally dried in a vacuum oven at 80 °C overnight. The biomass carbon materials derived from CS, PNS, PB, and MP were labeled as **C-CS**, **C-PNS**, **C-PB**, and **C-MP**, respectively.

For PNS, the activation process is carried out with KOH and H_3PO_4 as the activating agent, respectively. For KOH-activated PNS biomass, PNS and KOH (1 : 3, g g^{-1}) were dispersed in deionized water for 6 h, filtered, and dried in a vacuum oven at 80 °C for 48 h. For H_3PO_4-activated PNS biomass, PNS was dispersed in 60% H_3PO_4 solution (1 : 3, g mL^{-1}) for 6 h and filtered, and solids were collected, and then dried in an oven at 80 °C for 48 h. The activated PNS was pyrolyzed according to the above operations, and the biochar materials obtained were labeled as **C-K-PNS** and **C-P-PNS**, respectively. **C-P-PNS** at different pyrolysis temperatures can be labeled as **C-P-PNS-600**, **C-P-PNS-800**, and **C-P-PNS-1000**, respectively.

2.2. Preparation of the ODZ tablet sample

For preparing the ODZ sample, ten compound ODZ tablets were ground into a fine powder. Then, 25 mg of ODZ powder was completely dispersed in 100 mL of ethanol and acetonitrile-water (30 : 70, V/V), respectively, and adequately sonicated for 20 minutes. The obtained turbid liquid was slowly filtered through a microporous filtration membrane to remove the sediment, and the filtrate was collected for subsequent electrochemical detection and HPLC analysis. Detailed information about the reagents and apparatus used in the experiments are provided in the SI.

2.3. Live subject statement

All the urine samples used in the experiment were obtained from healthy adult volunteers. The collection of urine samples was carried out in accordance with the *Guidelines for the Collection and Handling of Urine Specimens*. All experiments were conducted in compliance with the relevant laws and guidelines of the People's Republic of China and were approved by Shenyang Key Laboratory of Medical Molecular Theranostic Probes in School of Pharmacy. Furthermore, informed consent was obtained for any experimentation with human subjects.

3. Results and discussion

3.1. Electrochemical reduction of ODZ at different electrodes

The intricate and multifunctional architectures of natural biomaterials position them as promising candidates for electrochemical sensing applications. First, we used cyclic voltammetry (CV) curves to compare the electrochemical detection performance of electrodes modified with different materials for ODZ. Fig. 1a illustrates the CV responses of 0.1 mM ODZ in 7.0 PBS at the bare GCE, **C-PNS/GCE**, **C-MP/GCE**, **C-PB/GCE**, and **C-CS/GCE**. Notably, almost no anodic peaks corresponding to ODZ were observed at any of the electrodes, indicating that the reduction reaction is completely irreversible. The electroreduction of ODZ at **C-PNS/GCE** exhibited a significantly higher peak current compared to that at **C-PB/GCE**, **C-CS/GCE**, and **C-MP/GCE**. To achieve a highly sensitive current response, **C-PNS** was designated as the sensing material for subsequent electrochemical detection. Furthermore, the electrochemical reduction performance of activated and unactivated **C-PNS** sensing materials towards ODZ was systematically compared. The comparison encompassed **C-K-PNS** and **C-P-PNS** samples. The CV curves of 0.1 mM ODZ at the bare GCE, **C-PNS/GCE**, **C-K-PNS/GCE**, and **C-P-PNS/GCE** are presented in Fig. 1b, S1 and S2. It is evident that **C-P-PNS/GCE** exhibited the highest reduction current of 15.16 μA, and a reduction peak potential of −0.574 V. The current response of **C-P-PNS/GCE** was 3.85 times higher than that of **C-PNS/GCE**, 1.90 times higher than that of **C-K-PNS/GCE**, and 2.81 times higher than that of the bare GCE. These results fully confirm that the reduction of ONZ on the **C-P-PNS/GCE** electrode is significantly enhanced.

3.2. Characterization of synthesized materials

The effects of different pyrolysis temperatures on the morphology of activated carbon materials were examined using SEM images. As illustrated in Fig. 2a, the surface of **C-P-NCS-600** exhibited a significant presence of massive particles, indicative of incomplete pyrolysis. In contrast, **C-P-NCS-800** displayed a fluffy and flocculent structure with an abundance of pore formations (Fig. 2b). When the pyrolysis temperature increased to 1000 °C, the porous structure partially collapsed, and the flocculent morphology became less pronounced (Fig. 2c). Through EDS energy spectra analysis and comparison, it can be known that with the increase in pyrolysis temperature, the proportion of phosphorus also increases (Fig. S3–S5 and Scheme 1).

The PXRD patterns of **C-P-PNS** at various pyrolysis temperatures are presented in Fig. 3a. It is evident that **C-P-PNS-600**, **C-P-PNS-800**, and **C-P-PNS-1000** exhibit two broad diffraction peaks at around 2θ values of 24° and 43°, which can be attributed to the 002 and 100 crystal planes of graphite, respectively.[26] These peaks indicate the disordered and amorphous characteristics inherent in all carbon materials. Notably, as the carbonization temperature increased, the intensity of the diffraction peak (002) diminished while that of the diffraction peak (100) intensified, suggesting an increase in internal defects within **C-P-PNS** following high-temperature pyrolysis.[27] The FT-IR spectra of **C-P-PNS-600**, **C-P-PNS-800**, and **C-P-PNS-1000** are presented in Fig. 3b. The absorption peak observed at 3440 cm^{-1} corresponds to the O–H stretching vibration.[28] The peak at 1585 cm^{-1} is attributed to the C=C stretching vibrations found in olefins and aromatics.[29] The peak at 1099 cm^{-1} belongs to the C–O stretching vibrations associated with phenolic and alcoholic groups.[29] In the spectra of **C-P-PNS-600** and **C-P-PNS-800**, the absorption peaks near 1120 cm^{-1} may correspond to P=O, C–O, or P=OOH stretching vibrations.[30] Notably, the intensity of the absorption peak in the spectrum of **C-P-PNS-800** is lower than that of **C-P-PNS-600** due to polyphosphate evaporation during pyrolysis temperature elevation.[31] Conversely, it is possible that no distinct absorption peak is present for **C-P-PNS-1000** because excessive pyrolysis temperatures may lead to evaporation and loss of the carbon-phosphorus skeleton.[31] Additionally, the absorption peaks at 937 cm^{-1} and 720 cm^{-1} belong to out-of-plane bending and stretching vibrations of C–H bonds within the benzene ring, which represents new bonds formed during H_3PO_4 activation.[32]

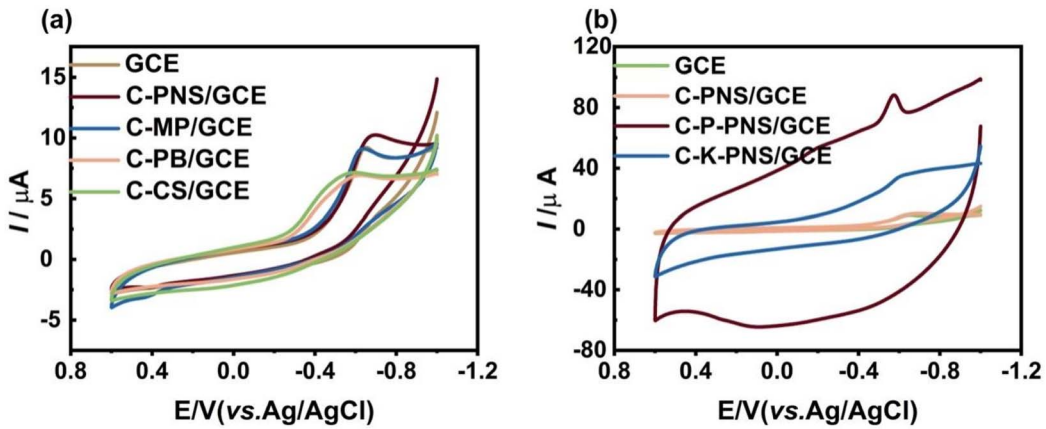

Fig. 1 (a) CVs of 100 μM ODZ on the GCE, **C-PNS/GCE**, **C-MP/GCE**, **C-PB/GCE**, and **C-CS/GCE** in 0.1 M PBS (pH = 7.0) and (b) CVs of 100 μM ODZ on the GCE, **C-PNS/GCE**, **C-P-PNS/GCE**, and **C-K-PNS/GCE** in 0.1 M PBS (pH = 7.0).

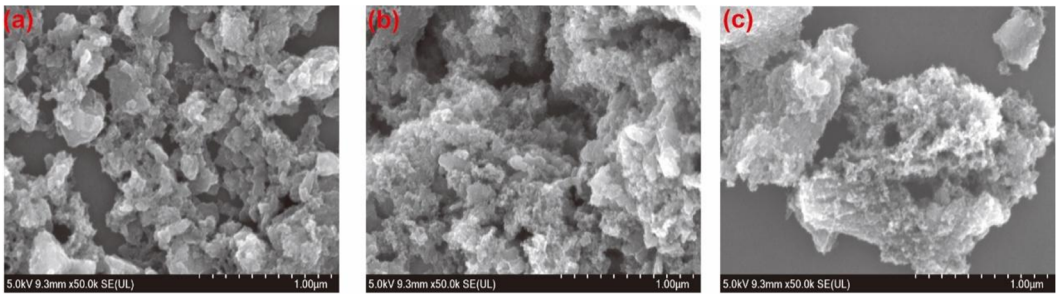

Fig. 2 SEM images of C-P-PNS-600 (a), C-P-PNS-800 (b) and C-P-PNS-1000 (c).

The N_2 adsorption–desorption isotherms of **C-P-PNS** obtained at three pyrolysis temperatures are shown in Fig. 3c. According to the IUPAC classification, **C-P-PNS-600**, **C-P-PNS-800**, and **C-P-PNS-1000** are all categorized as type IV isotherms.[24,33] When the relative pressure (P/P_0) was less than 0.1, the amount of N_2 adsorbed increased steadily, indicating a few micropores within the porous structure. Conversely, when the relative pressure (P/P_0) exceeded 0.4, the presence of a hysteresis loop suggested an abundance of mesoporous structures.[34] As shown in Fig. 3d, the pore sizes of **C-P-PNS-600**, **C-P-PNS-800**, and **C-P-PNS-1000** were calculated according to the density functional theory (DFT) method to be 1.68, 1.68, and 2.19 nm, respectively. **C-P-PNS-800** shows a specific surface area of 1317.84 $m^2\ g^{-1}$, and this result was much higher than 964.85 $m^2\ g^{-1}$ for **C-P-PNS-600** and 1019.93 $m^2\ g^{-1}$ for **C-P-PNS-1000** calculated by the Brunauer–Emmett–Teller (BET) method. The parameters related to pore structure are summarized in Table S1. Notably, **C-P-PNS-800** exhibited the smallest pore diameter, and the largest specific surface area and pore volume as well as an extensive pore structure. Additionally, in order to compare the performance characteristics of **C-PNS** before and after activation, **C-PNS-800** that underwent no activation treatment was also characterized using XRD, FT-IR, and N_2 adsorption–desorption techniques (Fig. S7–S10). The characterization results indicate that the P element content in unactivated C-PNS-800 is low, and its specific surface area is relatively small. Consequently, there remains a need for improvement in its electrochemical performance.

Pine nut shells are primarily composed of lignin, cellulose, hemicellulose, and inorganic salts. Lignin exhibits greater thermal stability compared to both hemicellulose and cellulose. At pyrolysis temperatures exceeding 600 °C, cellulose and hemicellulose were completely pyrolyzed, which significantly enhanced the relative proportions of lignin and inorganic salt components.[35] Lignin is a three-dimensional polymer formed from three phenylpropane units linked by C=O bonds and C–C bonds. It possesses abundant aromatic ring structures that facilitate the development of graphite microcrystalline formations.[36] Under appropriate pyrolysis conditions, it can yield amorphous carbon.[26] Inorganic salts possess distinct crystal structures that contribute to an increased specific surface area and porosity of the material, thereby offering additional pathways for electron transfer. Furthermore, following activation with phosphoric acid (H_3PO_4), polyphosphate groups are introduced into the pine nut shells; these groups gradually evaporated as the pyrolysis temperature increased, leading to

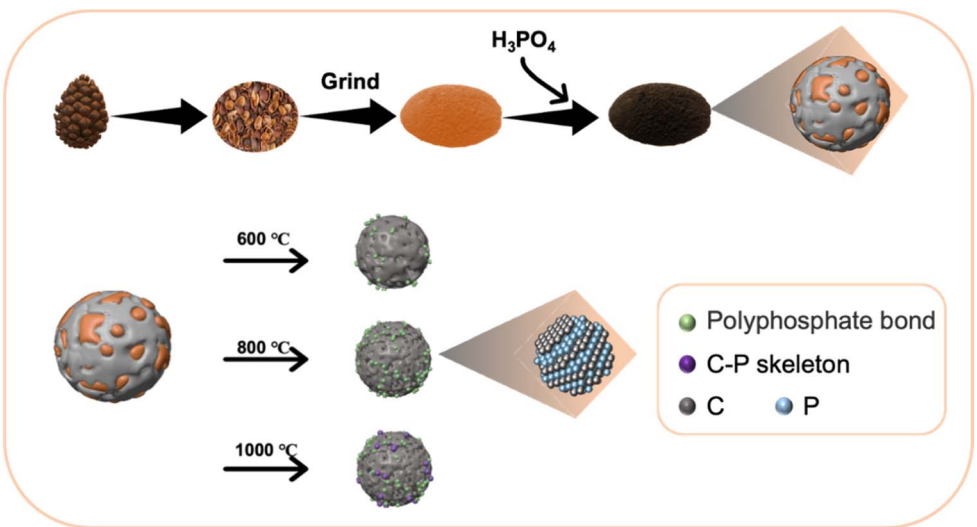

Scheme 1 Preparation process diagram of C-P-PNS and the effect of pyrolysis temperature on the morphology and composition of the carbon nanomaterial.

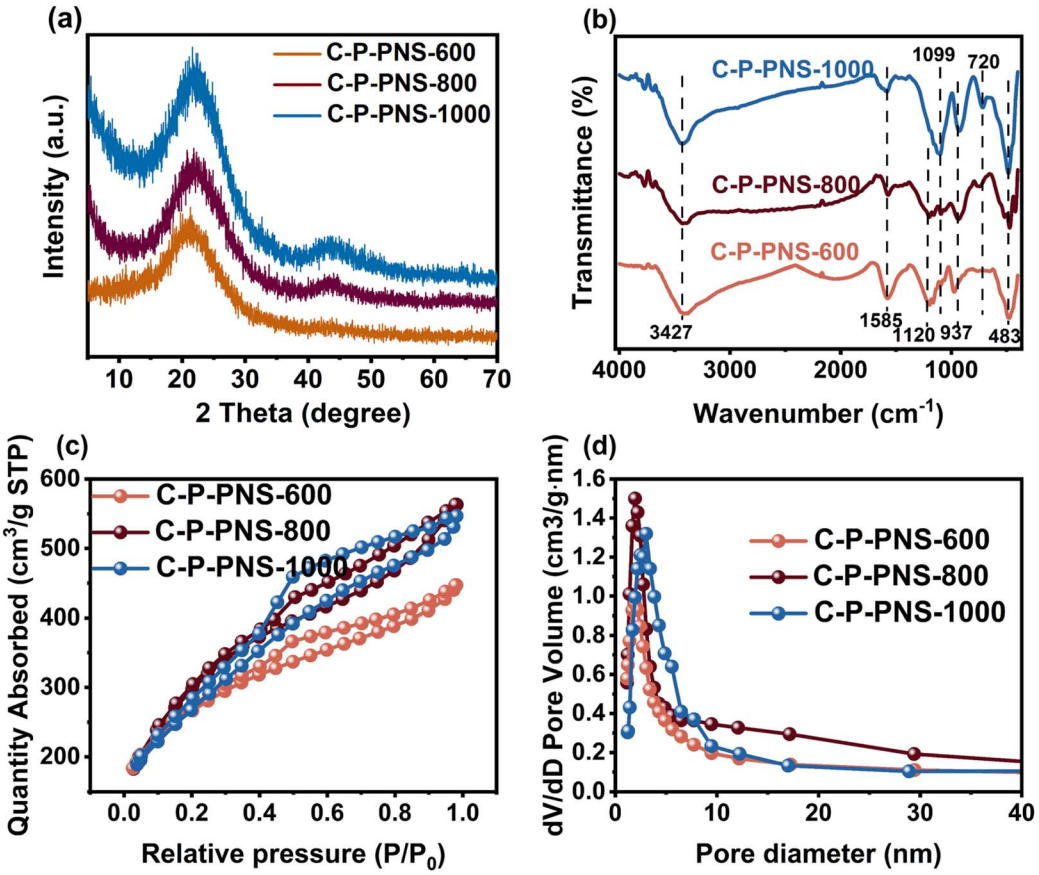

Fig. 3 (a) PXRD patterns and (b) FT-IR spectra of C-P-PNS-600, C-P-PNS-800 and C-P-PNS-1000; (c) N_2 adsorption–desorption isotherms, and (d) pore size distributions of C-P-PNS-600, C-P-PNS-800 and C-P-PNS-1000.

significant enhancements in the surface structure. **C-P-PNS-600** primarily comprised lignin and exhibited no distinct crystalline structure. During the pyrolysis process, the polyphosphate bonds decomposed, resulting in a material featuring small specific surface area and pore volume. In contrast, **C-P-PNS-800** demonstrated an obvious enhancement in the above aspects. These improvements were attributed to the evaporation of polyphosphate during pyrolysis and the condensation of aromatic rings due to lignin decomposition.[37] After pyrolysis at 1000 °C, the lignin degradation resulted in an increase in inorganic salt content of **C-P-PNS-1000**, leading to enhanced crystallinity.[38] Concurrently, the C–P framework vaporized, causing a significant reduction in the pore structure. Ultimately, the synergistic interaction between lignin, inorganic salts, and polyphosphate bonds in **C-P-PNS-800** leads to an optimized pore structure and increased specific surface area, facilitating efficient electron transport. Consequently, **C-P-PNS-800** exhibited superior electrochemical performance, making it an ideal candidate for electrode materials.

3.3. Electrochemical performance characterization of modified electrodes

The EIS technique was carried out in a 5 mM $K_3/K_4[Fe(CN)_6]$ solution containing 0.1 M KCl to explore the interface characteristics of the bare GCE, **C-P-PNS-600**, **C-P-PNS-800**, and **C-P-PNS-1000**. The high-frequency semicircular region in the Nyquist plots (Fig. 4a) is associated with the charge transfer resistance (R_{ct}). Based on the Randles circuit model (the inset of Fig. 4a), the R_{ct} values of the GCE, **C-P-PNS-600**, **C-P-PNS-800**, and **C-P-PNS-1000** were calculated to be 130.40, 8.95, 5.74, and 7.67 Ω, respectively. It is clear that the R_{ct} value of the bare GCE is the highest, indicating that the electron transfer rate of $[Fe(CN)]_6^{3-/4-}$ on the surface of the GCE is the lowest. The high frequency semicircle diameters of the GCE modified with **C-P-PNS** materials are obviously reduced, which indicates that **C-P-PNS** has excellent electrical conductivity and has great potential as an electrode modification material. Among them, **C-P-PNS-800** has the lowest R_{ct} value, accelerating electron transfer, which is related to its unique pore size and composition formed at an optimum pyrolysis temperature. The existence of a small amount of micropores contributes to increasing the specific surface area and enriching the adsorption sites for ions. The presence of a significant number of mesopores facilitates the reduction of ion diffusion distance, thereby decreasing diffusion resistance. This enhancement allows ions to access micropores more effectively, which in turn reduces charge transfer resistance and improves electrical conductivity performance.[39] Therefore, C-

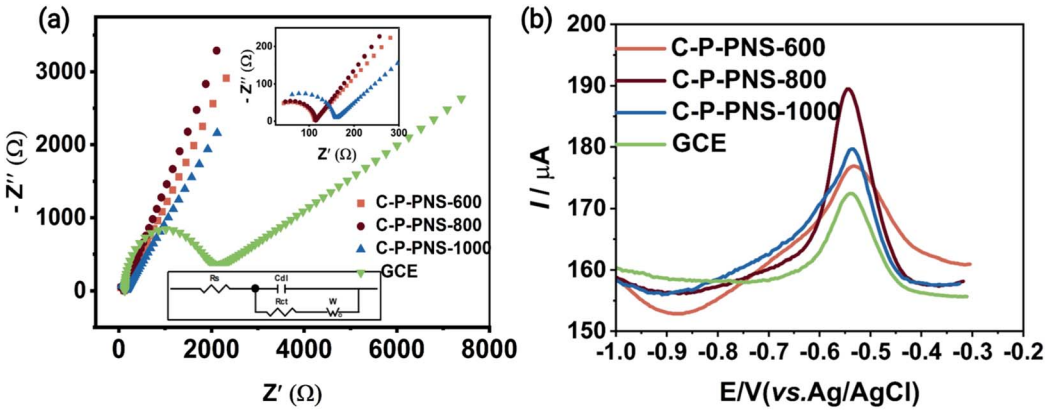

Fig. 4 (a) Nyquist plots of the bare GCE, **C-P-PNS-600**, **C-P-PNS-800**, and **C-P-PNS-1000** (inset: Randles equivalent circuit model); (b) DPV curves of the bare GCE, **C-P-PNS-600/GCE**, **C-P-PNS-800/GCE**, and **C-P-PNS-1000/GCE** in pH 7.0 PBS solution containing 100 μM ODZ.

P-PNS-800 is expected to develop into a novel electrochemical sensing material.

3.4. Investigation of electrochemical behavior for ODZ

The electrochemical reduction reactions of the GCE, **C-P-PNS-600/GCE**, **C-P-PNS-800/GCE**, and **C-P-PNS-1000/GCE** for 100 μM ODZ were analyzed using the differential pulse voltammetry (DPV) method. As illustrated in Fig. 4b, the GCE exhibited a weak response current of 15.60 μA, indicating a slow electron transfer rate on its surface. In contrast to the GCE, **C-P-PNS-600/GCE**, **C-P-PNS-800/GCE**, and **C-P-PNS-1000/GCE** electrodes demonstrated significantly higher response signals of 19.79, 31.99, and 28.87 μA, respectively. This suggests that **C-P-PNS** biomass carbon possesses excellent electrocatalytic activity for ODZ reduction. Furthermore, the **C-P-NCS-800/GCE** electrode displayed the highest reduction current because of its larger specific surface area and increased number of active sites. Consequently, **C-P-NCS-800** was selected as the optimal electrode material for subsequent experimental studies for detecting ODZ.

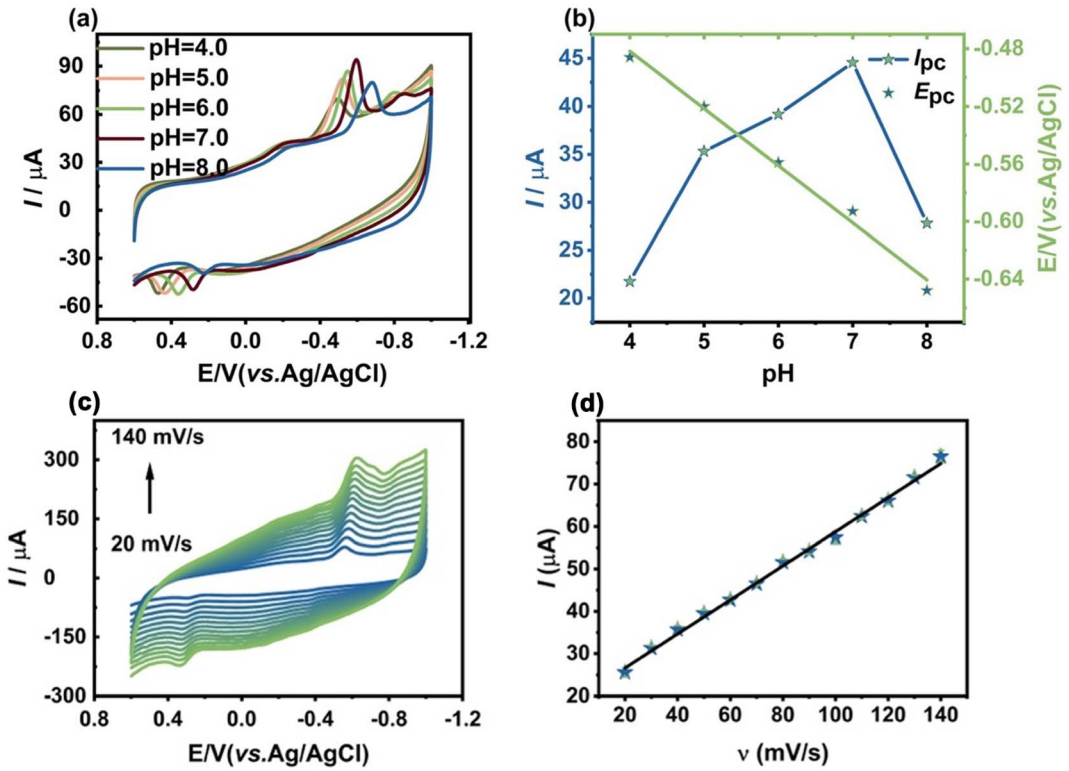

Fig. 5 (a) CV graphs of 100 μM ODZ on the **C-P-PNS-800/GCE** electrode at various pH levels (4.0–8.0) in 0.1 M PBS; (b) the plots of I_{pc} and E_{pc} with pH; (c) CV curves of **C-P-PNS-800/GCE** at various scanning rates (ranging from 20 mV s^{-1} to 140 mV s^{-1}) in 0.1 M PBS (pH = 7.0) including 100 μM ODZ; (d) the relationship between I_{pc} and v.

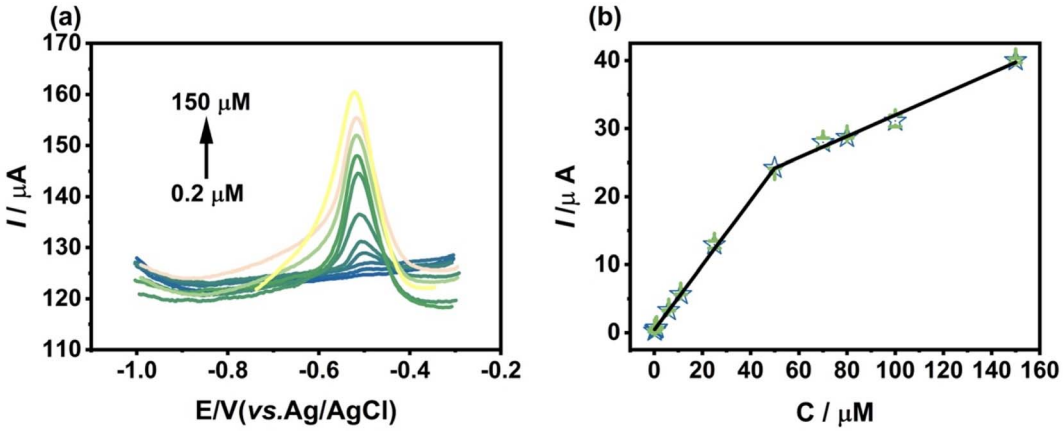

Fig. 6 (a) DPV response of C-P-PNS-800/GCE with increasing of ODZ from 0.2–150 μM; (b) corresponding linear plots of ODZ concentration *vs.* current response.

3.5. Optimization of ODZ detection parameters

3.5.1. Effect of pH and scan rate. For the **C-P-PNS-800/GCE** system, electrochemical investigations of ODZ redox behavior were conducted in PBS buffer solution with varying pH values (4.0 to 8.0) using the CV technique. As presented in Fig. 5a, the oxidation and reduction peak current values progressively increased as the pH values of the buffer solution increased from 4.0 to 7.0. Conversely, the oxidation and reduction peak currents decreased as the pH value increased from 7.0 to 8.0. The strongest current responses appeared at pH 7.0, leading to the PBS buffer solution with pH 7.0 being used for subsequent electrochemical detection. Moreover, the cathode peak potential (E_{pc}) shifted negatively as the pH value increased (Fig. 5b), indicating that ODZ protonated at the electrode–electrolyte interface. A linear correlation between E_{pc} and pH was established, and expressed by using the equation of $E_{pc} = -0.04$ pH + 0.32 ($R^2 = 0.9911$). Based on this relationship, the m/n ratio during the reduction process was calculated to be approximately 0.5. As shown in Fig. 5c, the electrochemical kinetics of **C-P-PNS-800/GCE** was studied using CV at a scanning rate of 20∼140 mV s^{-1}. The results show that the reduction current (I_{pc}) of ODZ increased linearly with the increase in the scanning rate (ν). As can be seen from Fig. 5d, the peak current intensity is proportional to the scanning rate, and its linear equation is I_{pc} (μA) = 0.403 ν (mV s^{-1}) + 18.563 ($R^2 = 0.9965$), indicating that the electrode surface has adsorption control kinetics for ODZ. The possible electrochemical reaction mechanism of ODZ on a modified sensor is discussed in the SI.

3.5.2. Influence of accumulation potential and accumulation time. In a PBS buffer solution (pH 7.0) containing 100 μM ODZ, DPV technology was employed to systematically investigate and optimize the accumulation potential and accumulation time for enhancing the sensing performance of the **C-P-PNS-800/GCE** electrode. Fig. S13a illustrates the effect of accumulation potential on the reduction peak current of ODZ. The results indicate that the accumulation potential of −0.3 V achieved the highest current response, which may be due to its proximity to the reduction potential of ODZ. Consequently, −0.3 V was selected as the optimal accumulation potential. Furthermore, Fig. S13b demonstrates the variation of ODZ reduction peak current with accumulation time on the **C-P-PNS-800/GCE** electrode. Over 240 seconds, no significant changes in the current response were observed, suggesting that adsorption equilibrium had been reached. In order to obtain higher detection sensitivity, subsequent experiments utilized an accumulation time of 240 s at an accumulation potential of −0.3 V.

3.6. Quantitative detection of ODZ

The DPV method with high sensitivity was employed to evaluate the quantitative detection capability of the **C-P-PNS-800/GCE** electrochemical sensor for ODZ. In a 0.1 M PBS solution at pH 7.0, the reduction peak current demonstrated a consistent increase with increasing ODZ concentration within the range of 0.2 to 150 μM, presenting two linear relationships (Fig. 6a and b). The calibration equations are I_{pc} (μA) = 0.48 + 0.28 C (0.2–50 μM, $R^2 = 0.9999$) and I_{pc} (μA) = 0.15 + 16.46 C (50−150 μM, $R^2 = 0.9913$). Based on these equations, the limit of detection (LOD) and limit of quantitation (LOQ) for ODZ were calculated to be 0.05 and 0.16 μM, respectively. Table 1 lists the performance of the **C-P-PNS-800/GCE** sensor compared with other electrochemical sensors used for ODZ detection.[15,40–44] It is evident that the **C-P-PNS-800/GCE** sensor has the characteristics of simple operation, high efficiency, and environmental friendliness, which is well-suited for the quantitative detection of ODZ.

Table 1 Comparison of the reported ODZ sensor with different electrocatalysts and methods

Electrodes	Linear range (μM)	Detection limit (μM)	Ref.
DTU-67 and T-PPY	0–250.4	0.25	15
p-ABSA/GCE	0.8–50.0	0.10	40
dsDNA/GCE	2.5–37.5	0.80	41
Polyfurfural-rGO/GCE	1–50.0	0.25	42
Au-AuNR/AE	3.0–500.0	0.18	43
Co_3O_4/SnO_2/GCE	0.2–1185.8	0.06	44
C-P-PNS-800/GCE	0.2–150.0	0.05	This work

3.7. Repeatability, stability, anti-interference, and cycling performance

In a PBS buffer solution containing 100 μM ODZ (pH = 7.0), DPV was employed to evaluate the repeatability, stability, anti-interference capability, and cycling performance of the **C-P-PNS-800/GCE** electrode. Five identical **C-P-PNS-800/GCE** electrodes were utilized to measure the current responses, yielding a relative standard deviation (RSD) of 2.4% (Fig. 7a and b). Additionally, the RSD of the same electrode was 0.94% after 6 consecutive detections (Fig. 7c and d). To assess the stability of the electrode material, the current responses were measured every three days with the same electrode over a 21-day period. After this duration, the reduction peak current remained at 95% of the initial value (Fig. 7e). Therefore, the above experiments verify that **C-P-PNS-800/GCE** displays excellent repeatability and stability. The current signals of the ODZ solution in the presence of various inorganic salt ions (100 times K^+, Na^+, Cl^-, PO_4^{3-}, and SO_4^{2-}), organic molecules in body fluids (50 times glucose, lysine, sucrose, citric acid, and ascorbic acid), as well as structural analogs (equal concentrations of nitrofurazone and metronidazole) are illustrated in Fig. 7f. The relative errors in the current responses were less than 5%, indicating high selectivity for ODZ detection in the presence of interfering substances. Finally, the cycling performance of the electrode

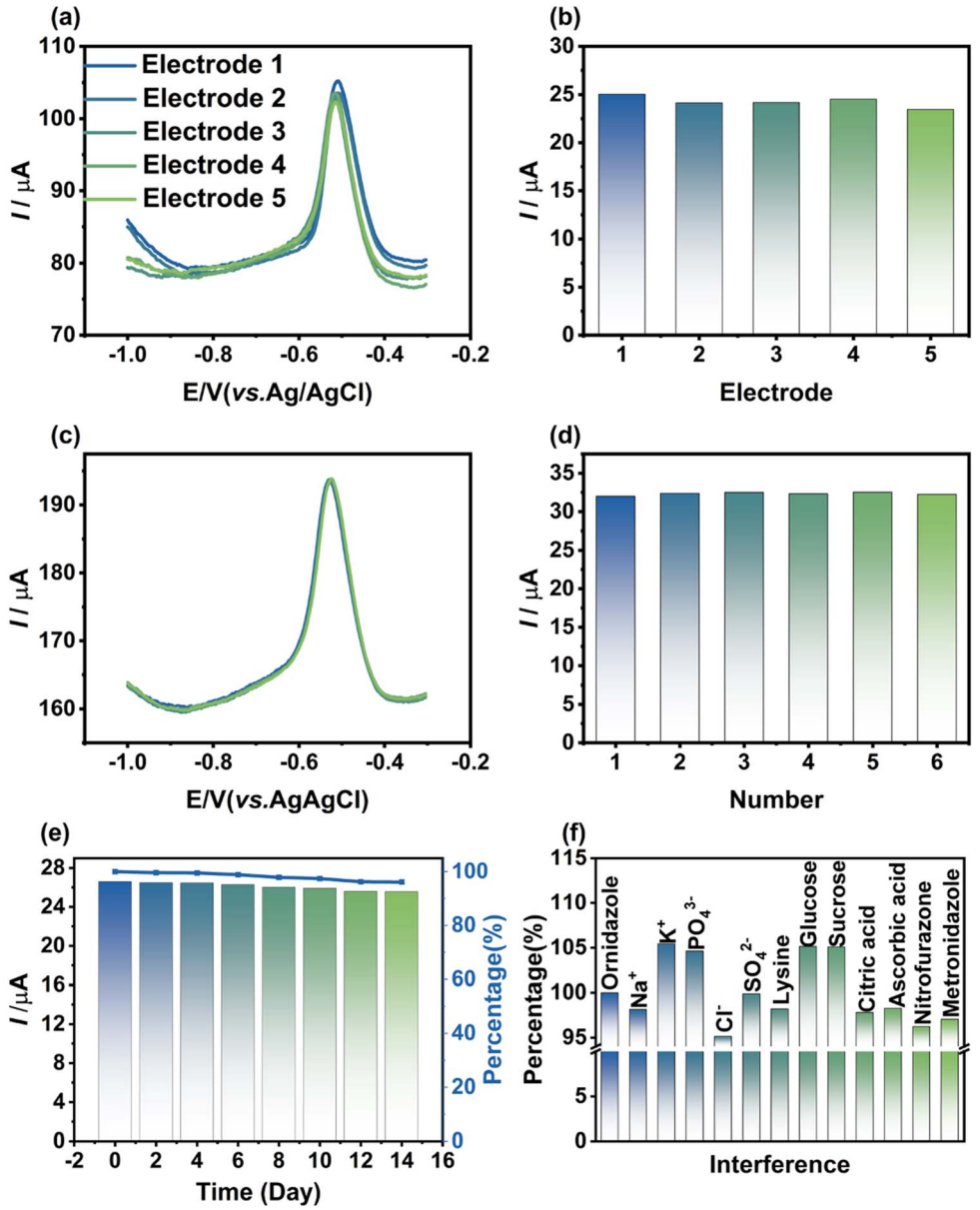

Fig. 7 (a and b) Reproducibility study of 100 μM ODZ detected by five different C-P-PNS-800/GCE electrodes; (c and d) repeatability study of 100 μM ODZ for six tests conducted on the same C-P-PNS-800/GCE electrode; (e) the stability study of the C-P-PNS-800/GCE electrode; (f) the anti-interference ability of the C-P-PNS-800/GCE electrode in the presence of different interfering substances.

Table 2 The results of ODZ content in actual samples by using the C-P-PNS-800/GCE sensor

		C-P-PNS-800/GCE		
Real sample	Added (μM)	Found (μM)	Recovery (%)	RSD ($n = 3$)
Ornidazole tablets	0.00	55.26	—	0.64
	20.00	76.00	103.70	2.52
	30.00	86.12	102.87	1.21
	40.00	95.19	99.83	0.65
Human urine	0.00	0.00	—	—
	20.00	19.32	96.60	2.54
	30.00	31.27	104.23	1.95
	40.00	40.58	101.45	2.72

was evaluated. It can be seen that the current response of the **C-P-PNS-800/GCE** electrode decreased to 95% of the initial current after 32 consecutive cycles in the ODZ solution, confirming its reusability for multiple cycles (Fig. S14).

3.8. Application of actual samples

To assess the practicality of the **C-P-PNS-800/GCE** electrode, the content of ODZ in ornidazole tablets and human urine was detected by DPV analysis using the standard addition method. As displayed in Table 2, the recovery values of the electrochemical methods are between 96.60% and 104.23% with the RSD less than 3%. Concurrently, the content of ODZ in tablets was determined by HPLC for evaluating the accuracy of the determination results by using the **C-P-PNS-800/GCE** sensor. Under the external standard method, the test results obtained by the two methods are exhibited in Table S2. The independent sample *T*-test reveals no significant difference ($P > 0.05$), which signifies that the electrochemical sensor based on **C-P-PNS-800/GCE** can realize the accurate detection of ODZ.

4. Conclusions

In summary, a novel strategy was successfully exploited for synthesizing waste biomass-derived porous carbon materials. Pine nut shells were utilized as the raw material source, H_3PO_4 served as the activator, and a carbonization temperature of 800 °C was employed. This material was subsequently applied to the electrochemical detection of ODZ with remarkable success. The synthesized **C-P-PNS-800** exhibits a specific surface area of 1317.84 $m^2\ g^{-1}$, a pore volume of 0.92 $cm^3\ g^{-1}$, and an average pore size of 1.68 nm, which significantly enhances electron conductivity. When used to modify glassy carbon electrodes, **C-P-PNS-800** demonstrated excellent electrochemical responses, characterized by an excellent sensitivity (0.48 μA μM^{-1}), a broad detection range (0.2–150 μM), as well as an ultralow detection limit (0.05 μM). Furthermore, the **C-P-PNS-800/GCE** system showed satisfactory reproducibility, repeatability, stability, selectivity, and recyclability in the detection of ODZ. It was reasonably used for analyzing ODZ in ornidazole tablets and human urine, yielding results which were not significantly different from those obtained by HPLC. This research not only provides a feasible approach for designing efficient electrochemical sensing systems based on waste plant-derived biomass but also opens new avenues for ODZ detection in pharmaceutical applications.

Author contributions

Chang Liu designed the experimental plan, conducted the experiments, organized the data, and contributed to the writing of the paper. Tianlong Shan prepared the figures and assisted with manuscript editing. Yuxiang Yang was responsible for the synthesis and characterization of the materials. Mengmeng Ding summarized and organized the experimental data, while Rui Zhang reviewed the manuscript content.

Conflicts of interest

The authors declare that they have no known competing financial interests or personal relationships that could have appeared to influence the work reported in this paper.

Data availability

The data supporting this article have been included as part of the SI. Supplementary information: reagents and instruments; construction of modified electrodes; electrochemical parameters; HPLC parameters; reaction mechanism; characterization of materials; electrochemical test figures, *etc.* See DOI: **https://doi.org/10.1039/d5ay01069a**.

Acknowledgements

This research was supported by the Natural Science Foundation of Liaoning Province (2025-BS-0251 and 2025-MS-295) and the Foundation of Liaoning Province Education Administration in 2024 (Independent topic selection–Natural science category–Strategic industrialization project LJ212410163023).

References

1 A. M. A. Salam, S. K. Rani, H. Patel, M. Pal, C.-Y. Kuo, M. Govindasamy and N. Vasimalai, *ACS Appl. Mater. Interfaces*, 2025, **17**, 7679–7696.
2 W. Wu, X. Wu, M. He, X. Yuan, J. Lai and H. Sun, *RSC Adv.*, 2021, **11**, 22993–23001.
3 J. Ganesamurthi, X.-R. Chen, R.-S. Juang, S.-Y. Wei and D.-Y. Lin, *J. Ind. Eng. Chem.*, 2023, **127**, 270–282.
4 H. J. Wang, D. Qian, X. L. Xiao, B. He, S. Q. Gao, H. Shi, L. F. Liao and J. Deng, *Electrochim. Acta*, 2017, **246**, 338–347.
5 L. Glennon, T. N. Barwa, D. Alves and C. B. Breslin, *J. Environ. Chem. Eng.*, 2025, **13**, 115578.
6 C. Koventhan, V. Vinothkumar and S.-M. Chen, *New J. Chem.*, 2021, **45**, 12593–12605.
7 F. E. Ettadili, M. Azriouil, M. Matrouf, O. T. Alaoui, F. Laghrib, A. Farahi, M. Bakasse, S. Saqrane, S. Lahrich and M. A. El Mhammedi, *Inorg. Chem. Commun.*, 2022, **140**, 109416.

8 M. Ikbal, G. Yilmaz, H. Dogan, M. Y. Alp and A. H. Cebi, *Drug Chem. Toxicol.*, 2011, **34**, 162–166.
9 M. Mehrzad-Samarin, F. Faridbod and M. R. Ganjali, *Spectrochim. Acta, Part A*, 2019, **206**, 430–436.
10 F. Chen, S. Y. Li, J. D. Peng, X. Wang, H. J. Peng, Y. Chen and Y. He, *Microchem. J.*, 2018, **141**, 423–430.
11 S. Z. Tan, C. G. Niu, J. H. Jiang, G. L. Shen and R. Q. Yu, *Anal. Sci.*, 2005, **21**, 967–971.
12 L. Y. Zhang, Z. J. Zhang and K. Wu, *J. Pharm. Biomed. Anal.*, 2006, **41**, 1453–1457.
13 K. Venkatesh, R. Rajakumaran, S.-M. Chen, C. Karuppiah, C.-C. Yang, S. K. Ramaraj, M. A. Ali, F. M. A. Al-Hemaid, M. S. El-Shikh and B. M. A. Almunqedhi, *Chemosphere*, 2021, **273**, 129665.
14 C. Bhuvaneswari and S. G. Babu, *Microchem. J.*, 2023, **193**, 109120.
15 H. Wang, X. Bo, M. Zhou and L. Guo, *Anal. Chim. Acta*, 2020, **1109**, 1–8.
16 C. Ragumoorthy, N. Nataraj, S.-M. Chen, G. Kiruthiga and X.-E. Phang, *Process Saf. Environ. Prot.*, 2025, **196**, 106927.
17 X. Niu, J. Yang and J.-F. Ma, *Sens. Actuators, B*, 2023, **387**, 133819.
18 J. Zhou, Q. Lou, Y. Li, Y. J. Zhang, G. P. Zeng, R. Lv, J. Li, J. Lan, Y. R. Li and Z. S. Zhao, *Electroanalysis*, 2025, **37**, e70011.
19 N. Balahmar, A. S. Al-Jumialy and R. Mokaya, *J. Mater. Chem. A*, 2017, **5**, 12330.
20 Y. Zhang, S. Liu, X. Zheng, X. Wang, Y. Xu, H. Tang, F. Kang, Q.-H. Yang and J. Luo, *Adv. Funct. Mater.*, 2017, **27**, 1604687.
21 D. S. Achilleos, W. X. Yang, H. Kasap, A. Savateev, Y. Markushyna, J. R. Durrant and E. Reisner, *Angew. Chem., Int. Ed.*, 2020, **59**, 18184–18188.
22 F. L. Lai, Y.-E. Miao, L. Z. Zuo, H. Y. Lu, Y. P. Huang and T. X. Liu, *Small*, 2016, **12**, 3235–3244.
23 S. J. Yu, J. K. He, Z. Zhang, Z. H. Sun, M. Y. Xie, Y. Q. Xu, X. Bie, Q. H. Li, Y. G. Zhang, M. Sevilla, M.-M. Titirici and H. Zhou, *Adv. Mater.*, 2024, **36**, 2307412.
24 C. Liu, L. Lv, Y. Sun and X. Di, *Microporous Mesoporous Mater.*, 2024, **374**, 113143.
25 Z. Z. Lv, X. L. Li, X. J. Chen, X. Li, M. Wu and Z. G. Li, *ACS Appl. Energy Mater.*, 2019, **2**, 8767–8782.
26 H. Guo, K. Sun, Y. X. Lu, H. L. Wang, X. B. Ma, Z. Y. Li, Y.-S. Hu and D. F. Chen, *Chin. Phys. B*, 2019, **28**, 068203.
27 Z. P. Tang, J. M. Gao, Y. Zhang, Q. Du, D. D. Feng, H. M. Dong, Y. R. Peng, T. H. Zhang and M. Xie, *Fuel Process. Technol.*, 2023, **241**, 107613.
28 F. Q. Guo, X. C. Jiang, X. P. Jia, S. Liang, L. Qian and Z. H. Rao, *J. Electroanal. Chem.*, 2019, **844**, 105–115.
29 S. L. P. Dias, C. L. Neto, V. G. Ferreira, J. C. P. Vaghetti, G. B. Machado and O. Bianchi, *Biomass Convers. Biorefin.*, 2024, **15**, 5975–5995.
30 I. I. G. Inal, S. M. Holmes, E. Yagmur, N. Ermumcu, A. Banford and Z. Aktas, *J. Ind. Eng. Chem.*, 2018, **61**, 124–132.
31 Y. J. Kan, Q. Y. Yue, J. J. Kong, B. Y. Gao and Q. Li, *Chem. Eng. J.*, 2015, **260**, 541–549.
32 L. Y. Qin, Z. W. Hou, S. H. Zhang, W. Zhang and E. C. Jiang, *J. Electroanal. Chem.*, 2020, **866**, 114140.
33 H. M. Lee, K.-H. An, S.-J. Park and B.-J. Kim, *Nanomaterials*, 2019, **9**, 608.
34 J. Du, L. Liu, Z. P. Hu, Y. F. Yu, Y. Zhang, S. L. Hou and A. B. Chen, *ACS Sustain. Chem. Eng.*, 2018, **6**, 4008–4015.
35 R. Tabakaev, I. Kalinich, I. Dimitryuk, A. Asilbekov, A. Astafev, K. Ibraeva, I. Shanenkov, A. Mostovshchikov and P. Chumerin, *J. Anal. Appl. Pyrol.*, 2023, **176**, 106264.
36 D. Y. Chen, K. H. Cen, X. Z. Zhuang, Z. Y. Gan, J. B. Zhou, Y. M. Zhang and H. Zhang, *Combust. Flame*, 2022, **242**, 112142.
37 M. H. Chen, F. Q. Luo, Y. C. Liao, C. R. Liu, D. W. Xu, Z. Wang, Q. Liu, D. Wang, Y. Y. Ye, S. R. Li, D. C. Wang and Z. F. Zheng, *J. Electroanal. Chem.*, 2022, **919**, 116526.
38 Z. Tang, R. Zhang, H. Y. Wang, S. Y. Zhou, Z. Y. Pan, Y. C. Huang, D. Sun, Y. G. Tang, X. B. Ji, K. Amine and M. H. Shao, *Nat. Commun.*, 2023, **14**, 6024.
39 Y. H. Cao, K. L. Wang, X. M. Wang, Z. R. Gu, Q. H. Fan, W. Gibbons, J. D. Hoefelmeyer, P. R. Kharel and M. Shrestha, *Electrochim. Acta*, 2016, **212**, 839–847.
40 G. Saglikoglu and S. Yilmaz, *Curr. Anal. Chem.*, 2014, **10**, 457–464.
41 Y. N. Ni, P. Wang and S. Kokot, *Biosens. Bioelectron.*, 2012, **38**, 245–251.
42 F. Ye, J. Z. Huang, Y. Q. Xu, Q. Zeng, J. M. Nan and L. S. Wang, *Anal. Lett.*, 2018, **51**, 728–741.
43 A. Rahi, N. Sattarahmady, R. D. Vais and H. Heli, *Sens. Actuators, B*, 2015, **210**, 96–102.
44 C. Koventhan, V. Vinothkumar and S.-M. Chen, *New J. Chem.*, 2021, **45**, 12593–12605.

